

Two temperature model for thermoacoustic sound generation in thick porous thermophones

Cite as: J. Appl. Phys. **126**, 165111 (2019); <https://doi.org/10.1063/1.5121395>

Submitted: 25 July 2019 . Accepted: 10 October 2019 . Published Online: 28 October 2019

Pierre Guiraud, Stefano Giordano , Olivier Bou Matar, Philippe Pernod, and Raphael Lardat



View Online



Export Citation



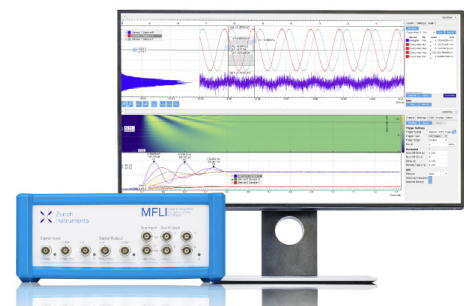
CrossMark

Challenge us.

What are your needs for periodic signal detection?



Zurich
Instruments



Two temperature model for thermoacoustic sound generation in thick porous thermophones

Cite as: J. Appl. Phys. **126**, 165111 (2019); doi: [10.1063/1.5121395](https://doi.org/10.1063/1.5121395)

Submitted: 25 July 2019 · Accepted: 10 October 2019 ·

Published Online: 28 October 2019



View Online



Export Citation



CrossMark

Pierre Guiraud,^{1,2,3,a)} Stefano Giordano,^{1,b)}  Olivier Bou Matar,¹ Philippe Pernod,¹ and Raphael Lardat²

AFFILIATIONS

¹Univ. Lille, CNRS, Centrale Lille, ISEN, Univ. Valenciennes, UMR 8520—IEMN, LIA LICS/LEMAC, F-59000 Lille, France

²Thales Underwater System France, Sophia Antipolis, 525 Route des Dolines, F-06560 Valbonne, France

³CINTRA UMI 3288, CNRS/NTU/THALES, Research Techno Plaza, 50 Nanyang Drive 637553, Singapore

^{a)}Electronic mail: pierre.guiraud@centraliens-lille.org

^{b)}Electronic mail: stefano.giordano@univ-lille.fr

ABSTRACT

Thermoacoustic sound generation offers a promising wideband alternative to mechanically driven loudspeakers. Over the past decade, the development of nanomaterials with new physicochemical properties promoted wide interest in thermophone technology. Indeed, several thermophone structures based on suspended nanowires, graphene sheets, highly porous foams, or sponges have been investigated. At the same time, theoretical models have been developed to predict the frequency and power spectra of these devices. However, most of the models have taken into consideration a solid homogeneous material for representing the thermophone generating layer, and its microstructure was, therefore, neglected. If this assumption holds for thin dense materials, it is not acceptable for thick and porous thermophone devices. Hence, a model able to describe the behavior of highly porous foam- or spongelike generating layers is proposed. It is based on a two-temperature scheme since the thermal equilibrium is not typically attained between the foam material and the embedded air. To do this, the fluid equations for the air are coupled with the heat equation for the solid foam through boundary conditions mimicking the energy exchange at the contact surface between them. The behavior of the main physical variables within the porous generating layer is explained and comparisons with recent experimental results are thoroughly discussed.

Published under license by AIP Publishing. <https://doi.org/10.1063/1.5121395>

I. INTRODUCTION

For now more than a century, sound generation has been realized by means of electroacoustic transducers, which are able to convert an electrical signal into sound waves. In the classical scheme, a coil/magnet core induces the vibration of a membrane, eventually generating an acoustic wave. Also, piezoelectric materials are used for sound generation in specific situations, such as underwater applications or buzzer devices. For both magnetic and piezoelectric systems, the operating principle is based on mechanical vibrations generating sound. Despite the huge technological improvements of those technologies over the past century, some limitations remain. Indeed, mechanically based sound generation is a resonant phenomenon meaning that a single loudspeaker is not able to achieve a wideband response.

In the early 20th century, an alternative solution has been proposed by Lange,¹ Arnold and Crandall,² and Wentz.³ They observed and theorized the thermoacoustic sound generation phenomenon.

This is based on a material having a low heat capacity and a high thermal and electrical conductivity. Whenever an electrical oscillating current is applied to the sample, its temperature follows the current variations, and the air in the vicinity of the sample will experience compression and dilatation processes, thus generating a sound wave (see Fig. 1). Due to the low efficiency of this principle and the limited availability of suitable materials, thermoacoustic sound generation was not largely exploited at that time. More recently, an efficient thermophone device made of a thin aluminum film deposited on a porous silicon substrate has been realized and analyzed.⁴ From then on, the development of advanced nanotechnologies strongly promoted the rapid progress of the thermoacoustic applications. Indeed, over the past two decades, many potential thermophones have been proposed and investigated. Without any pretension to being exhaustive, one could cite: thermophones with suspended nanowires (made of aluminum,⁵ gold,⁶ or silver⁷), graphene thermophones (based on

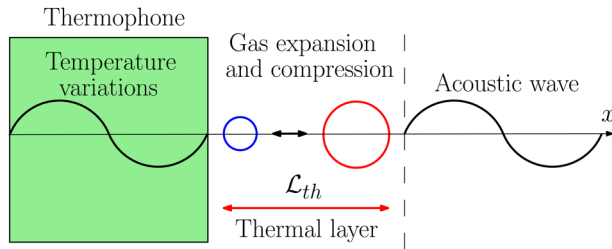


FIG. 1. Schematic of the thermoacoustic sound generation through thermophone devices.

paper technology,⁸ foam structures,⁹ or laser scribing¹⁰), and multi-walled nanotube (MWNT) devices.¹¹

The modeling of the thermoacoustic phenomena is important to analyze the behavior and design the structure of the thermophone systems. The original theory proposed by Arnold and Crandall² was generalized in order to take into consideration the heat stored by the thermophone material.¹² Later, energy based models have been used to describe the performances of thermophones deposited on a substrate.^{13,14} Also, the balance laws of continuum mechanics have been used to elaborate models for planar,¹⁵ cylindrical,¹⁶ and spherical thermophones.¹⁷ The same approach has been adopted to study the plane wave propagation in different thermophone configurations, such as the free field geometry¹⁸ and the thermophone on the substrate with an air gap.¹⁹ Lastly, a multi-layer model taking the wave propagation in the solid thermophone layer into account has been proposed.²⁰

In most models, the generating thermophone layer is considered as a homogeneous solid material. Consequently, the performances of the device are typically written in terms of the so-called heat capacity per unit area (HCPUA), which is defined as the product of the thickness of the layer L_s , its density ρ_s , and its heat capacity $C_{v,s}$. It is unanimously considered as the most important parameter describing the thermophone performances. It should be strongly reduced for obtaining an efficient thermoacoustic generation. This principle is well verified for dense and thin film thermophones. However, new thick foamlke materials assembled by chemical vapor deposition (CVD) are gaining interest because of their good efficiency and their higher mechanical stability.²¹ In spite of the interesting features of these materials, exhibiting a porosity larger than about 90%, no theoretical model exists to accurately describe their behavior. Therefore, a two-temperature model is presented here in order to gain a deeper insight into the thermoacoustic behavior of thermophones based on highly porous foamlke materials. This model introduces the local nonequilibrium between the temperatures of the solid foam and the air embedded inside it.^{22–26} It means that two different temperatures are considered for each phase of the generating layer. The balance equations for the air are coupled with the heat equation for the foam through a set of boundary conditions describing the exchange of energy at each contact surface between air and foam. This is the most important difference between our model and previous ones: while in previous models, the heat exchange between generating layer and air occurs only at the

two external surfaces, in the present case, the actual distribution of air within the pores and the heat exchanges at any foam-air contact are considered. This process is able to explain the high efficiency observed in real thermophones based on foam- or spongelike materials. A complete description of the main physical variable inside the generating layer is given together with a comparison between experimental and theoretical results for both thin film thermophones and thick porous thermophones.

The paper is structured as follows. In Sec. II, the two-temperature theory can be found and a technique to solve the main equations in the case of a thermophone radiating planar waves in free field is proposed. In Sec. III, an acoustic diffraction theory, based on the classical Rayleigh’s second integral, is introduced and used later on to draw a comparison with experimental results. In Sec. IV, the behavior of the most important physical variables is analyzed in order to clarify the thermoacoustic processes in a porous structure. Then, the two-temperature model is compared with previous models and with experimental data taken from the recent literature. For the sake of completeness, the models are applied to both thin film thermophones and thick porous thermophones.

II. TWO-TEMPERATURE THEORETICAL MODEL FOR A THERMOPHONE IN FREE FIELD

The general conservation equations for mass, linear momentum, and energy in a fluid medium can be written as²⁷

$$\frac{1}{B} \frac{\partial p}{\partial t} - \alpha_T \frac{\partial T}{\partial t} + \vec{\nabla} \cdot \vec{v} = 0, \quad (1)$$

$$\rho \frac{\partial \vec{v}}{\partial t} = -\vec{\nabla} p + \mu \nabla^2 \vec{v} + (\lambda + \mu) \vec{\nabla} (\vec{\nabla} \cdot \vec{v}), \quad (2)$$

$$\rho C_p \frac{\partial T}{\partial t} - \alpha_T T_0 \frac{\partial p}{\partial t} = \kappa \nabla^2 T, \quad (3)$$

where the pressure $p(\vec{r}, t)$ (pascal), the temperature variation $T(\vec{r}, t)$ (kelvin), and the particle velocity vector $\vec{v}(\vec{r}, t)$ (m/s) are the main variables depending on time t (seconds) and position vector \vec{r} (meters). Moreover, ρ is the density (kg/m^3), B is the bulk modulus (pascal), α_T is the coefficient of volumetric expansion ($1/\text{K}$), λ and μ the first and second viscosity coefficients (Pa s), C_p is the specific heat at constant pressure [$\text{J}/(\text{kg K})$], T_0 is the ambient temperature (kelvin) and, finally, κ is the thermal conductivity [$\text{W}/(\text{m K})$]. All these parameters will be considered as constants for a given fluid medium. These equations represent the linearized motion of the fluid around the equilibrium state identified by $T = T_0$, $p = p_0$, and $\vec{v} = 0$.

To begin, a thermophone radiating in free field is considered, as shown in Fig. 2. The central active layer of the thermophone is assumed to be made of a porous material with a very high porosity (e.g., larger than 90%), with an undeformable solid microstructure. Therefore, a model is elaborated to take into account the effect of the fluid (typically air) embedded within the pores of the active solid phase, i.e., the coupling between the fluid and the micro- or nanostructured porous solid in the active region. The fluid motion within the pores of the thermophone region can be described by Eqs. (1)–(3). However, due to the possible high frequency of the

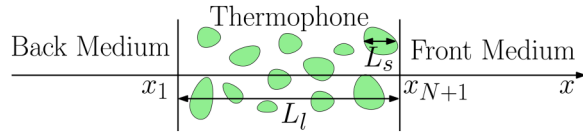


FIG. 2. Schematic of a porous thermophone radiating in free field (symmetrically in back and front media). The thermophone layer has a width L_l and foam branches of average diameter L_s . The volumetric source S_0 is supplied to the foam structure by the Joule effect.

electric energy supplied, the local thermal equilibrium is not attained between fluid and solid phases. Therefore, the conservation equations in the fluid can be coupled with the energy conservation for the solid phase, where an input power density S_0 is introduced (Joule effect), and a temperature $T_s \neq T$ is considered. The combination of such equations represents the nonthermal equilibrium between fluids and solids. In other terms, since the temperatures of fluid and solid are sensibly different on the two sides of a real contact interface, a phenomenological two-temperature model has to be considered to effectively take account of this nonthermal equilibrium. Moreover, to better take into consideration the morphology of the porous structure within the generation layer, an exchange of energy at the contact surfaces between pores and foam branches is introduced. This scheme can be mimicked by a series of interfaces, which are represented in Fig. 3. Each layer is, therefore, described by the following set of equations:

$$\frac{1}{B} \frac{\partial p}{\partial t} - \alpha_T \frac{\partial T}{\partial t} + \vec{\nabla} \cdot \vec{v} = 0, \quad (4)$$

$$\rho \frac{\partial \vec{v}}{\partial t} = -\vec{\nabla} p + \mu \nabla^2 \vec{v} + (\lambda + \mu) \vec{\nabla}(\vec{\nabla} \cdot \vec{v}), \quad (5)$$

$$\rho C_p \frac{\partial T}{\partial t} - \alpha_T T_0 \frac{\partial p}{\partial t} = \kappa \nabla^2 T, \quad (6)$$

$$\rho_s C_{v,s} \frac{\partial T_s}{\partial t} = \kappa_s \nabla^2 T_s + S_0, \quad (7)$$

where the last equation represents the added energy conservation in the solid foam and the subscript s is used for the solid/foam parameters. For instance, $C_{v,s}$ is the specific heat at constant

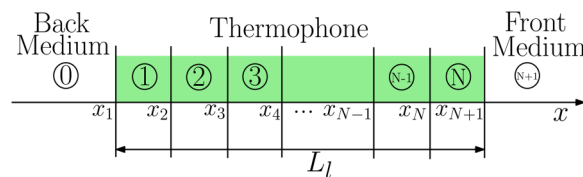


FIG. 3. Two-temperature representation of the porous thermophone. In each layer, a temperature T is associated with the air within the pores, and a temperature $T_s \neq T$ is associated with the foam branches. The interfaces control the energy exchange between foam and air.

volume of the foam $[J/(kg K)]$. For the sake of simplicity, this system is investigated in the one-dimensional case (plane wave propagation along the x axis) with an harmonic time dependence. Then, one obtains

$$\frac{i\omega}{B} p - i\omega \alpha_T T + \frac{dv}{dx} = 0, \quad (8)$$

$$i\omega \rho v = -\frac{dp}{dx} + (\lambda + 2\mu) \frac{d^2 v}{dx^2}, \quad (9)$$

$$i\omega \rho C_p T = \kappa \frac{d^2 T}{dx^2} + i\omega \alpha_T T_0 p, \quad (10)$$

$$i\omega \rho_s C_{v,s} T_s = \kappa_s \frac{d^2 T_s}{dx^2} + S_0, \quad (11)$$

where i is the imaginary unit. Importantly, in these equations, the terms $\rho_s C_{v,s}$ and κ_s must be considered as the homogenized values over the whole volume of the generation layer. Indeed, the two-temperature model implicitly considers two effective phases (air and foam, in our case), both occupying the whole region of the thermophone layer. Therefore, for each phase, the homogenized values for all physical properties have to be considered.^{22–26} However, since the materials display a very high porosity, the homogenized parameters are adopted only for the foam phase.

The energy exchange between air in the pores and solid branches is written in the boundary conditions that are summarized below. To write these conditions, the definition of the heat flux is introduced in the air phase as $q = -\kappa dT/dx$ and in the solid foam phase as $q_s = -\kappa_s dT_s/dx$. Moreover, instead of considering the pressure p , the normal surface tension \tilde{p} is adopted as $\tilde{p} = p - (\lambda + 2\mu)dv/dx$, which takes into account the viscous stress. Now, in each layer of the thermophone (layers from 1 to N , see Fig. 3), there are four variables \tilde{p} , v , T , and q for the air and two variables T_s and q_s for the branches. On the other hand, in the back and front media (layers 0 and $N + 1$), there are only the variables for the air, namely, \tilde{p} , v , T , and q . An index $0 \leq i \leq N + 1$ is associated with these variables to identify the layer where they are defined. For the interfaces within the thermophone (from x_2 to x_N), one has

$$\tilde{p}_{i-1}(x_i) = \tilde{p}_i(x_i), \quad (12)$$

$$v_{i-1}(x_i) = v_i(x_i), \quad (13)$$

$$T_{i-1}(x_i) = T_i(x_i), \quad (14)$$

$$T_{s,i-1}(x_i) = T_{s,i}(x_i), \quad (15)$$

$$q_i(x_i) = q_{i-1}(x_i) + g(T_{s,i}(x_i) - T_i(x_i)), \quad (16)$$

$$q_{s,i}(x_i) = q_{s,i-1}(x_i) - g(T_{s,i}(x_i) - T_i(x_i)), \quad (17)$$

for all $i = 2, \dots, N$. While the first four relations represent the classical continuity of normal stress, velocity, and temperatures, the last two relations represent the energy exchanged between solid

branches and air. Indeed, if $T_{s,i}(x_i) \geq T_i(x_i)$, a positive quantity of energy leaves the foam and moves to the surrounding air. This process is controlled by a new parameter g [W/(m² K)], describing the fluid/solid coupling at the interfaces. Concerning the first interface at x_1 (back medium/thermophone), the result is

$$\tilde{p}_0(x_1) = \tilde{p}_1(x_1), \tag{18}$$

$$v_0(x_1) = v_1(x_1), \tag{19}$$

$$T_0(x_1) = T_1(x_1), \tag{20}$$

$$q_1(x_1) = q_0(x_1) + g(T_{s,1}(x_1) - T_1(x_1)), \tag{21}$$

$$q_{s,1}(x_1) = -g(T_{s,1}(x_1) - T_1(x_1)), \tag{22}$$

and, finally, the last interface equation at x_{N+1} (thermophone/front medium) is written as

$$\tilde{p}_N(x_{N+1}) = \tilde{p}_{N+1}(x_{N+1}), \tag{23}$$

$$v_N(x_{N+1}) = v_{N+1}(x_{N+1}), \tag{24}$$

$$T_N(x_{N+1}) = T_{N+1}(x_{N+1}), \tag{25}$$

$$q_{N+1}(x_{N+1}) = q_N(x_{N+1}) + g(T_{s,N}(x_{N+1}) - T_N(x_{N+1})), \tag{26}$$

$$0 = q_{s,N}(x_{N+1}) - g(T_{s,N}(x_{N+1}) - T_N(x_{N+1})). \tag{27}$$

It is interesting to observe that this proposed two-temperature model differs from the classical two-temperature model described in the literature.^{22–26} Indeed, in our case, the exchange of energy is confined at all interfaces representing the contacts between air and foam. This process is not continuous and, therefore, it is not implemented within the balance equations defined in each layer [see Eqs. (8)–(11)]. On the other hand, it is important to also note that, in this thermophone model, the heating of the air is a process distributed (although not continuously) within the whole region of the generation layer (at all the air/foam contacts) and not only at the external interfaces (at x_1 and x_{N+1}) as in the classical thermophone models.²⁰ For this reason, it is able to represent the behavior of thick and porous thermophone devices.

The solution for the physical variables defined in each layer of the model can be found as follows. From Eq. (8), the pressure can be obtained as

$$p = \alpha_T B T - \frac{B}{i\omega} \frac{dv}{dx}. \tag{28}$$

Then, the normal surface tension \tilde{p} becomes

$$\tilde{p} = \alpha_T B T - \left(\lambda + 2\mu + \frac{B}{i\omega} \right) \frac{dv}{dx}. \tag{29}$$

Using Eq. (29) along with Eqs. (8)–(11), the velocity is eventually

found as

$$v = -\frac{1}{i\omega\rho} \left[\alpha_T B + \frac{i\omega\rho C_v}{\alpha_T T_0 B} \left(\lambda + 2\mu + \frac{B}{i\omega} \right) \right] \frac{dT}{dx} + \left(\lambda + 2\mu + \frac{B}{i\omega} \right) \frac{\kappa}{i\omega\rho\alpha_T T_0 B} \frac{d^3 T}{dx^3}, \tag{30}$$

where the thermodynamic relationship between the specific heats $\rho(C_p - C_v) = T_0\alpha_T^2 B$ has been used. The fourth-order differential equation for T can be then found in the form

$$0 = \left(\lambda + 2\mu + \frac{B}{i\omega} \right) \kappa \frac{d^4 T}{dx^4} - \omega^2 \rho^2 C_v T - \left[\left(\lambda + 2\mu + \frac{B}{i\omega} \right) i\omega\rho C_v + (i\omega\rho\kappa + \alpha_T^2 T_0 B^2) \right] \frac{d^2 T}{dx^2}, \tag{31}$$

coherently with recent investigations.²⁰ The solutions of Eq. (31) represent thermal modes and acoustical modes that will be described by θ_{th} and k_{ac} , respectively. The temperature in the fluid can be, therefore, written as

$$T = A e^{-ik_{ac}x} + B e^{+ik_{ac}x} + C e^{-\theta_{th}x} + D e^{+\theta_{th}x}. \tag{32}$$

On the other hand, from the energy conservation in the solid, Eq. (11), the temperature T_s can be easily written as

$$T_s = E e^{-\theta_{solid}x} + F e^{+\theta_{solid}x} + T_{s,0}, \tag{33}$$

with $T_{s,0}$ being the particular solution of Eq. (11) given by

$$T_{s,0} = \frac{S_0}{\rho_s C_{v,s} i\omega}. \tag{34}$$

In previous solutions A, B, C, D, E , and F are constants to be determined. In order to obtain the values of θ_{th} and k_{ac} , the following parameters are introduced:

$$\gamma = \frac{C_p}{C_v}, \tag{35}$$

$$C_0 = \sqrt{\frac{B}{\rho}} \gamma, \tag{36}$$

$$l_k = \frac{C_0 \kappa}{B C_p}, \tag{37}$$

$$l_v = \frac{\lambda + 2\mu}{\rho C_0}. \tag{38}$$

In order to find the values of k_{ac} and θ_{th} , one should find the solutions of the algebraic fourth-order (biquadratic) characteristic equation associated with Eq. (31). Since the exact solutions are rather cumbersome, it is useful to assume a weak thermal conduction and a weak viscosity of the adopted medium. Under these hypotheses,

the asymptotic solutions of Eq. (31) can be obtained in the form

$$k_{ac} = \pm \frac{\omega}{C_0} \left[1 - \frac{i\omega}{2C_0} l_v - \frac{i\omega}{2C_0} l_k \left(1 - \frac{1}{\gamma} \right) \right], \quad (39)$$

$$\theta_{th} = \pm \sqrt{\frac{i\omega\gamma}{C_0 l_k}} \left[1 + \frac{i\omega}{2C_0} l_k \left(1 - \frac{1}{\gamma} \right) + \frac{i\omega}{2C_0} l_v (1 - \gamma) \right]. \quad (40)$$

While the detailed proof of Eqs. (39) and (40) is given in the recent literature,²⁰ it is worth noticing that these results represent the first order expansions (with small κ , λ , and μ) of the solutions of the algebraic equation associated with Eq. (31). For the air, this is a good approximation in the frequency range of interest for the thermophone applications. If necessary, the values of θ_{th} and k_{ac} can be obtained numerically, without any assumption on the material parameters. On the other hand, through Eq. (11), the propagation constant in the solid can also be found as

$$\theta_{solid} = \pm \sqrt{\frac{i\omega\rho_s C_{v,s}}{\kappa_s}}. \quad (41)$$

The set of solutions in a layer, concerning the air variables, is obtained as

$$\tilde{p} = A\mathcal{F}(-ik_{ac})e^{-ik_{ac}x} + B\mathcal{F}(ik_{ac})e^{ik_{ac}x} + C\mathcal{F}(-\theta_{th})e^{-\theta_{th}x} + D\mathcal{F}(\theta_{th})e^{\theta_{th}x}, \quad (42)$$

$$v = A\mathcal{G}(-ik_{ac})e^{-ik_{ac}x} + B\mathcal{G}(ik_{ac})e^{ik_{ac}x} + C\mathcal{G}(-\theta_{th})e^{-\theta_{th}x} + D\mathcal{G}(\theta_{th})e^{\theta_{th}x}, \quad (43)$$

$$q = A\kappa ik_{ac}e^{-ik_{ac}x} - B\kappa ik_{ac}e^{ik_{ac}x} + C\kappa\theta_{th}e^{-\theta_{th}x} - D\kappa\theta_{th}e^{\theta_{th}x}, \quad (44)$$

$$T = Ae^{-ik_{ac}x} + Be^{ik_{ac}x} + Ce^{-\theta_{th}x} + De^{\theta_{th}x}, \quad (45)$$

where the functions

$$\mathcal{F}(\eta) = \alpha_T B - \left(\frac{B}{i\omega} + \lambda + 2\mu \right) (L_1 \eta^2 + L_2 \eta^4), \quad (46)$$

$$\mathcal{G}(\eta) = L_1 \eta + L_2 \eta^3 \quad (47)$$

have been introduced, with L_1 and L_2 being the coefficients [see Eq. (30)],

$$L_1 = -\frac{1}{i\omega\rho} \left[\alpha_T B + \frac{i\omega\rho C_v}{\alpha_T T_0 B} \left(\lambda + 2\mu - i\frac{B}{\omega} \right) \right], \quad (48)$$

$$L_2 = \left(\lambda + 2\mu - i\frac{B}{\omega} \right) \frac{\kappa}{i\omega\rho\alpha_T T_0 B}. \quad (49)$$

By defining the matrices

$$H^{(a)} = \begin{bmatrix} \mathcal{F}(-ik_{ac}) & \mathcal{F}(ik_{ac}) & \mathcal{F}(-\theta_{th}) & \mathcal{F}(\theta_{th}) \\ \mathcal{G}(-ik_{ac}) & \mathcal{G}(ik_{ac}) & \mathcal{G}(-\theta_{th}) & \mathcal{G}(\theta_{th}) \\ \kappa ik_{ac} & -\kappa ik_{ac} & \kappa\theta_{th} & -\kappa\theta_{th} \\ 1 & 1 & 1 & 1 \end{bmatrix} \quad (50)$$

and

$$H^{(b)}(x) = \begin{bmatrix} e^{-ik_{ac}x} & 0 & 0 & 0 \\ 0 & e^{ik_{ac}x} & 0 & 0 \\ 0 & 0 & e^{-\theta_{th}x} & 0 \\ 0 & 0 & 0 & e^{\theta_{th}x} \end{bmatrix}, \quad (51)$$

the general solution in a given fluid layer is given by

$$\begin{bmatrix} \tilde{p}_i(x) \\ v_i(x) \\ q_i(x) \\ T_i(x) \end{bmatrix} = H^{(a)} H^{(b)}(x) \begin{bmatrix} A_i \\ B_i \\ C_i \\ D_i \end{bmatrix}, \quad (52)$$

for all $0 \leq i \leq N + 1$. It is important to observe that the relations $A_0 = C_0 = B_{N+1} = D_{N+1} = 0$ must be imposed since no progressive wave in the back medium (identified by $i = 0$) and no regressive wave in the front medium (identified by $i = N + 1$) are considered. Similarly, the general solution for the solid/foam variables in a given layer is given by

$$\begin{bmatrix} q_{s,i}(x) \\ T_{s,i}(x) \end{bmatrix} = G(x) \begin{bmatrix} E_i \\ F_i \end{bmatrix} + \begin{bmatrix} 0 \\ T_{s,0} \end{bmatrix}, \quad (53)$$

for all $1 \leq i \leq N$. Here, the matrix

$$G(x) = \begin{bmatrix} \kappa_s \theta_{solid} e^{-\theta_{solid}x} & -\kappa_s \theta_{solid} e^{\theta_{solid}x} \\ e^{-\theta_{solid}x} & e^{\theta_{solid}x} \end{bmatrix} \quad (54)$$

is introduced. The knowledge of the complete solution of the problem for all the physical variables and all the layers [see Eqs. (52) and (53)] allows to implement the boundary conditions given in Eqs. (12)–(27). Indeed, it is not difficult to prove that these conditions are represented by $6N + 4$ linear equations, with exactly $6N + 4$ unknown coefficients. The system is well posed and can, therefore, always be solved by standard numerical methods.

Interestingly enough, the model stated in this section can be further improved by adding a term corresponding to the heat loss at the interfaces, which is described by a new coefficient β_s [W/(m² K)]. To introduce this effect, Eqs. (16), (21), and (26) must be substituted with

$$q_i(x_i) = q_{i-1}(x_i) + g(T_{s,i}(x_i) - T_i(x_i)) - \beta_s T_i(x_i), \quad (55)$$

$$q_1(x_1) = q_0(x_1) + g(T_{s,1}(x_1) - T_1(x_1)) - \beta_s T_1(x_1), \quad (56)$$

$$q_{N+1}(x_{N+1}) = q_N(x_{N+1}) + g(T_{s,N}(x_{N+1}) - T_N(x_{N+1})) - \beta_s T_N(x_{N+1}), \quad (57)$$

where the last term in each relation, described by the coefficient β_s , models the influence of conduction, convection, and radiation losses. The total loss is considered proportional to the temperature, and this represents a good approximation for losses due to conduction and convection. However, it is a poor representation of the radiated heat, which is typically proportional to the fourth power of the temperature. Nevertheless, the thermal losses by radiation in a thermophone are negligible in most of the cases.²⁸ More general approaches for considering imperfect interfaces can be found in the literature.^{29,30}

III. ACOUSTIC DIFFRACTION THEORY

The model here developed describes the thermoacoustic sound generation for a thermophone with a infinitely large surface, radiating in near field. However, real measurements are typically done in far field, with finite size thermophones. Therefore, an acoustic diffraction theory must be implemented to compare the results of our model with experiments. If a planar surface at $x = x_0$, vibrating with the velocity $v(y, z)$, is studied, each point can be considered as an acoustic source. Hence, the actual pressure field can be found by superposition, using the classical Rayleigh's second integral,

$$p_{\text{FF}}(x, y, z) = \frac{i\omega\rho}{4\pi} \int_{-L_y}^{L_y} \int_{-L_z}^{L_z} v(y', z') \frac{e^{-ikr}}{r} dz' dy', \quad (58)$$

where $r = \sqrt{(x - x_0)^2 + (y - y')^2 + (z - z')^2}$ is the distance between generation and observation points, with (x, y, z) being the coordinates of the observation point and (x_0, y', z') those of the generation point. The rectangle $(-L_y, L_y) \times (-L_z, L_z)$ represents the vibrating region of the plane. In order to use Eq. (58), the velocity field in air is calculated through our near field model for a distance from the thermophone slightly larger than the thickness of the thermal layer \mathcal{L}_{th} (active region), as defined in Fig. 1. Indeed, at this distance, the velocity has attained its maximum value, which can be considered for the acoustic propagation in Eq. (58). The thickness of the thermal layer has been evaluated through the approximated expression $\mathcal{L}_{th} = 2\sqrt{\frac{C_0 k}{2\omega\gamma}}$.²⁰ Hence, the theoretical curves that will be shown in Sec. IV represent the results of the Rayleigh's second integral applied to the velocity field of our near field model. In other words, our model is used to describe the thermoacoustic generation of waves, whereas the diffraction theory is used to properly take into account the resulting acoustic propagation.

IV. ANALYSIS AND COMPARISON WITH EXPERIMENTAL RESULTS

In Sec. II, a two-temperature model for the thermoacoustic sound generation has been elaborated. This model was motivated by the fact that most of the currently used thermophones are composed of noncontinuous materials. For instance, widely adopted structures are based on multiwalled nanotubes (MWNTs), arranged as sheets, forests, foams, or sponges.³¹ Those thermophones devices are, therefore, made of both air and nanotubes. Thus, the models based on a continuous homogeneous medium do not represent the real microstructure of these systems and neglect the interaction

fluid/solid in the active region. As a matter of fact, in foamlike thermophones, a porosity of the active layer as large as 99% can be achieved, making the air component not negligible.

In the following (see Sec. IV A), the thermoacoustically generated temperatures, particle velocity, and heat fluxes are analyzed as a function of the position x (one-dimensional modeling) at a frequency of 3 kHz. This allows for a deeper understanding of the model and a better interpretation of the thermoacoustic generation phenomena in porous devices.

Additionally, measurements published in the literature will be compared to the theoretical response of our two-temperature model (referred to as 2T model from now on) and of the classical model based on a homogeneous and solid active layer (referred to as 1T model from now on).²⁰ The comparison will be discussed in two distinct sections, dealing with different thicknesses of the thermophone. Section IV B will investigate thin film thermophones with thickness of a few micrometers and Sec. IV C foamlike thermophones with thickness of hundreds of microns. The experimental data are taken from a recent investigation.³¹ This work provides frequency and power spectra of a wide variety of samples with a full description of the experimental setup. Thermal parameters of the samples were also measured and discussed. These data have been used in the theoretical models, making the comparison theory/experiment legitimate.

All of the presented theoretical results have been obtained using the parameters in Tables I and II. A specific discussion concerns the parameter g , which is the only new parameter introduced in this model. The real total contact area between the solid foam and air is given by $a\rho_s V$, where a is the specific area of the foam (m^2/kg), ρ_s is the foam density (kg/m^3), and V is the total foam volume (m^3) (of course, $a\rho_s$ is the interfacial area per unit volume). On the other hand, the effective contact area introduced in our model is given by NS , where N is the number of layers in Fig. 2 and S is their area. On the basis of these premises, g can be defined as $NSg = a\rho_s Vh$, where h is the real heat film transfer coefficient [$\text{W}/(\text{m}^2 \text{K})$] (convective and radiative). One simply obtains $g = \frac{a\rho_s Vh}{NS} = \frac{a\rho_s hL_l}{N}$, where $L_l = V/S$. With the reasonable values $a = 1000\text{--}2000 \text{ m}^2/\text{g}$,^{32,33} $h = 200 \text{ W}/(\text{m}^2 \text{K})$,³⁴ $\rho_s = 30 \text{ kg}/\text{m}^3$, $L_l = 0.1\text{--}1 \text{ mm}$, and $N = 10$, one obtains $g \cong 10^5 \text{ W}/(\text{m}^2 \text{K})$, which is used throughout all the papers.

The 2T model and the classical 1T model,²⁰ based on a single homogeneous active layer, have been implemented (see Fig. 2). Both models have been adapted for acoustic diffraction as discussed in Sec. III, by considering the size and the shape of the samples used in the experimental activity.³¹ All results show the sound pressure level (SPL), defined in decibels (dB), and calculated as

$$\text{SPL} = 20 \log_{10} \left(\frac{p_{\text{rms}}}{p_{\text{ref}}} \right), \quad (59)$$

where p_{rms} is the root mean square pressure (i.e., $|p_{\text{FF}}|/\sqrt{2}$, where p_{FF} is the complex pressure introduced in previous sections) and p_{ref} is the reference sound pressure being, by definition, $20 \mu\text{Pa}$ in air. The results are shown at a distance of 3 cm from the thermophone. The frequency spectrum results are normalized with power and the power spectrum results are shown at 3 kHz.

TABLE I. Parameters of the propagating medium (air).

	ρ (kg m ⁻³)	C_p (J kg ⁻¹ K ⁻¹)	C_V (J kg ⁻¹ K ⁻¹)	B (Pa)	α_T (K ⁻¹)	κ (W K ⁻¹ m ⁻¹)	λ (N s m ⁻²)	μ (N s m ⁻²)
Gas, air	1.20	9.96×10^2	7.17×10^2	1.01×10^5	3.33×10^{-3}	26.2×10^{-3}	16.82×10^{-6}	5.61×10^{-6}

A. Behavior of the physical variables with the two-temperature model

Here, the behavior of the main physical variables is shown by comparing a thick and a thin thermophone. For the thick thermophone, the parameters of the graphene sponge ($L_l = 800 \times 10^{-6}$ m) are adopted, while for the thin one, the parameters of the CNT sheet ($L_l = 18 \times 10^{-6}$ m) are used. In Fig. 4, one can find the temperatures, the particle velocity, and heat fluxes vs x , calculated with the 1T and the 2T models for both the thick and thin thermophones at $f = 3$ kHz. In this figure, the curves corresponding to the absolute value of the different complex quantities have been plotted. To better explain the behavior of the heat flux within the system, in Fig. 5, the real and imaginary parts of the heat fluxes in air and foam are shown as well. The input power is the same for all curves (1 W) in Figs. 4 and 5. The geometry considered is shown in Fig. 3, where $N = 5$ is imposed to easily identify the pores/branches structure in the plots. Moreover, the diffraction procedure is not implemented to obtain the results of this section since only the near field generation is investigated. Please note that the 1T model gives the behavior of the physical quantities only outside the thermophone layer. On the contrary, the 2T model allows for the complete analysis, also in the generating porous structure.

Figures 4(a) and 4(b) show that despite a slightly higher value of the temperature on the edges of the thermophone for the 1T model, both thick and thin systems display the same behavior in air. The thermal active layer \mathcal{L}_{th} can be seen in the vicinity of the thermophone and has the same length in all cases since it only depends on the frequency and the propagating medium (the higher the frequency, the smaller the size of the generating layer). In the inset of Fig. 4(a), one can see that the temperatures inside the thin thermophone are almost constant and the branches providing the energy from the solid to the air in the 2T model are not distinguishable. On the other hand, for a thick thermophone, one can find in Fig. 4(b) the energy transmission near the branches, represented by the interfaces. Finally, it is seen that, in the thick thermophone, the temperature of the solid is higher at the center of the thermophone and local maxima also exist in between two branches. Importantly, these evaluations of the temperatures within the thermophone layer (pores and branches) can be performed only with the proposed 2T model. These results are

relevant for both analyzing the system and designing porous thermophones with specific features.

Figures 4(c) and 4(d) show the heat fluxes in the considered structures. As before, the 1T model presents higher values of q at the edge of the thermophone than the 2T model, but the same order of magnitude and behavior are observed in both models. The thin thermophone displays an almost continuous increase of q inside the thermophone, from the center to the external edges (2T model). However, for the thick thermophone, the heat flux transmission is seen in the air/foam structure and is characterized by a series of peaks. The sawtooth shape of the curves in Fig. 4(d) is due to the fact that the absolute value of complex quantities is shown. To better understand the behavior of the heat fluxes in the structure, the real and imaginary parts of these quantities are represented in Fig. 5, for both thin and thick thermophones. In the generating layer of the thin thermophone [panels (a) and (c) of Fig. 5], the exchange of energy at the contact zones between air and foam can be only slightly appreciated. However, concerning the thick thermophone [panels (b) and (d) of Fig. 5], one can clearly observe the jumps of the heat fluxes within the generating layer in both air and foam. These jumps represent the exchange of energy between air and foam and are described by Eqs. (16) and (17). It can be remarked that T in the air is not very different from T_s in the foam in the contact zones [see Fig. 4(b)]. Nevertheless, since the parameter g assume a quite large value, the product $g(T_s - T)$, characteristic of the two-temperature model, is always finite and positive and it can be seen [in panels (b) and (d) of Fig. 5] as the measure of the jumps in both q and q_s curves. Moreover, it is interesting to note that the jumps in q and q_s (both real and imaginary parts) are always of the same extent but in opposite directions. It is perfectly coherent with the idea of energy exchanges, as introduced in Eqs. (16) and (17).

Figure 4 [panel (e)] shows that, for a thin thermophone, the particle velocity within the 1T and the 2T models is of the same magnitude leading to a similar radiated SPL of about 110 dB in the vicinity of the thermophone. This is attributed to the fact that the density of branches is high enough for the temperature and the flux to be continuous in the thermophone leading the 2T model to perform similarly to the 1T one. On the other hand, in Fig. 4 [panel (f)], it is seen that the particle velocity assumes different

TABLE II. Parameters of the thermophone materials used in the experiments and theoretical models.³¹

	ρ_s (kg m ⁻³)	$C_{V,s}$ (J kg ⁻¹ K ⁻¹)	B_s (Pa)	κ_s (W K ⁻¹ m ⁻¹)	L_l (m)	L_s (m)	A (cm ²)
CNT sheet	1	716	1.11×10^{11}	50	18×10^{-6}	10×10^{-9}	Square 1.5×1.5
ITO PAN	220	606	1.65×10^{11}	310	5×10^{-6}	450×10^{-9}	Square 1.2×1.5
MWNT sponge	30	716	1.11×10^{11}	100	100×10^{-6}	10×10^{-9}	Square 1×1
Graphene sponge	2.75	660	1.44×10^8	6.3	800×10^{-6}	5×10^{-9}	Circle $d = 1.8$

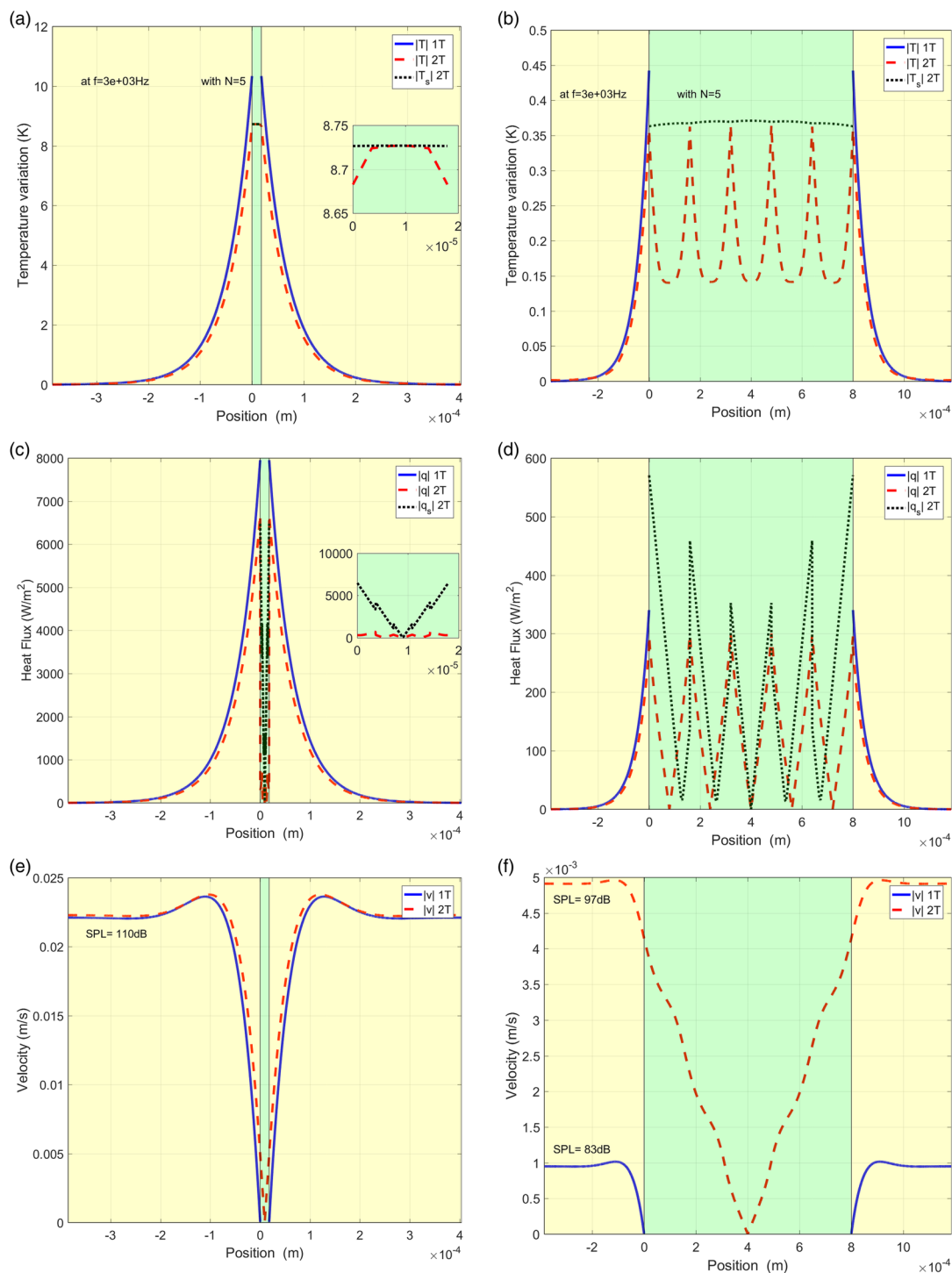


FIG. 4. Near field temperature variations [(a) and (b)], heat flux [(c) and (d)], and particle velocity [(e) and (f)] for a thin [(a), (c), and (e)] and thick [(b), (d), and (f)] thermophone. All parameters are plotted only in air with the 1T model and in both air and solid with the 2T model. All curves show the absolute value of the corresponding complex quantities. The central region (green) represents the thermophone layer with both air and solid foam and the regions on the left and on the right (yellow) represent the air layers. The insets in (a) and (c) show a zoom within the generating layer.

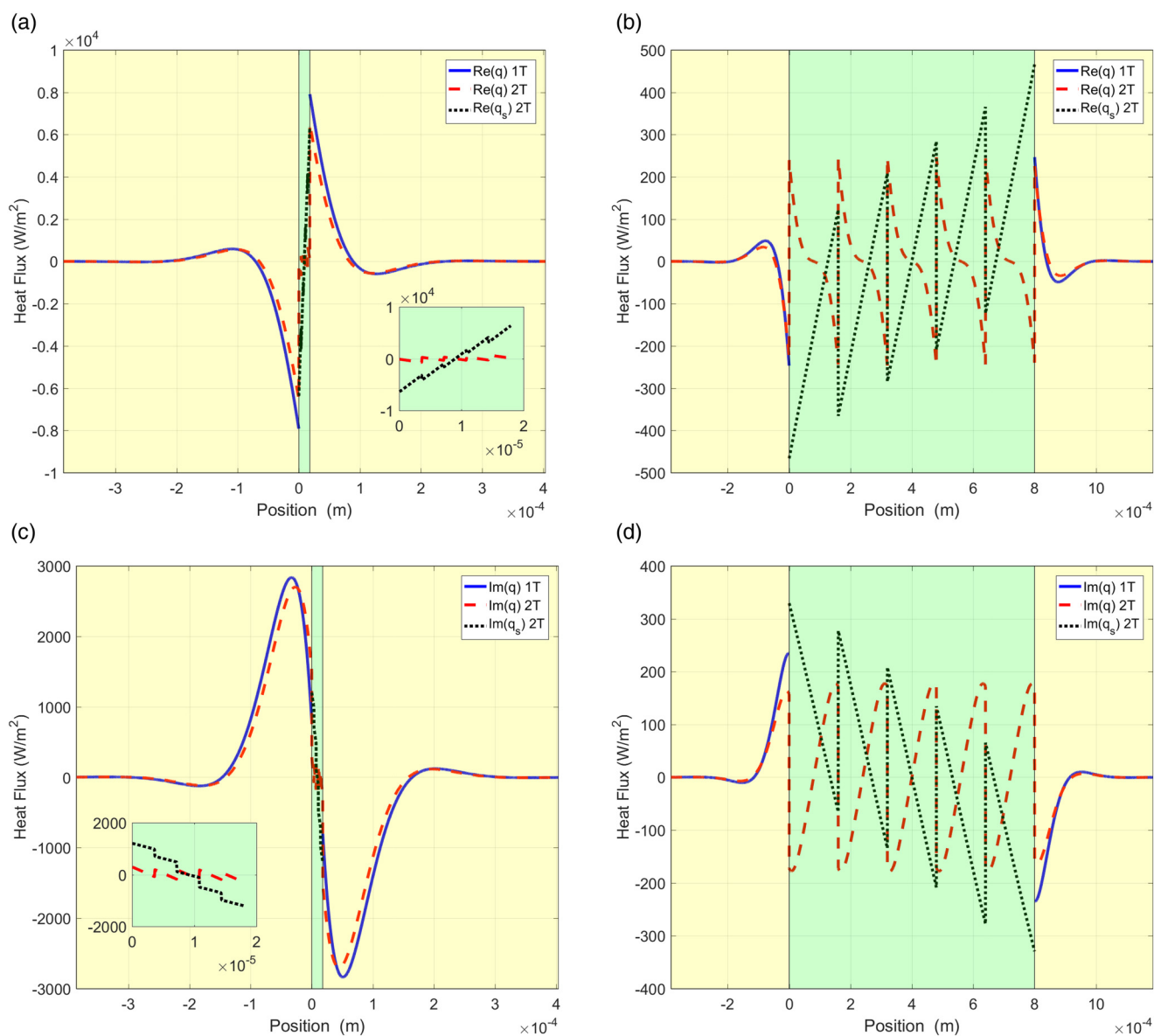


FIG. 5. Real part [(a) and (b)] and imaginary part [(c) and (d)] of the heat flux for a thin [(a) and (c)] and a thick [(b) and (d)] thermophone. The quantities are plotted only in air with the 1T model and in both air and solid with the 2T model. The central region (green) represents the thermophone layer with both air and solid foam and the regions on the left and on the right (yellow) represent the air layers. The insets in (a) and (c) show a zoom within the generating layer.

values for the 1T and the 2T models, leading to different radiated SPL of about 83 and 97 dB, respectively. This difference is attributed to the noncontinuity of the thermophone layer in the 2T model, in opposition to the bulk solid layer in the 1T model. The improvement of the performances is clearly proportional to N . From the physical point of view, it means that the crucial factor to improve the performances is the total surface contact between air and foam branches within the porous generating layer. Clearly, this total surface increases with porosity but also depends on the real

geometry of the microstructure (shape and connectivity of pores). The thick porous structure allows indeed to reduce the influence of the heat stored in the generating layer, thus improving the conversion of thermal energy in acoustic energy, e.g., the overall efficiency. This mechanism, properly implemented in the 2T model, corresponds to the actual behavior of real porous thermophones, as proved by the following comparisons with recent experiments.

In this section, it was seen that, for thin thermophones, the 2T model performs similarly to the 1T model, but this is not the case

with thicker and porous thermophones, where a sound generation difference of more than 10 dB is observed. This proves that the modeling of the generating layer is of primary importance and that the thermoacoustic generation is intricately linked to its geometry (size, microstructure, and so on). The theoretical model has, therefore, to be tuned to each thermophone geometry.

B. Thin film thermophones

Figures 6(a) and 6(b) show the frequency and the power response of a carbon nanotube sheet (CNT sheet) and an indium-tin oxide coated poly(acrylonitrile) nanofiber sheet (ITO PAN). In both cases, the diffraction procedure of Sec. III has been applied to the theoretical models. CNT sheets are considered as the most efficient thermophones currently available because of the very low heat capacity per unit area (HCPUA) induced by their low density and low specific heat.³¹ For this reason, CNT sheets are considered as the reference nanostructures for thermoacoustic heaters.³¹ On the contrary, ITO PAN devices have a much higher density and, therefore, a higher HCPUA leading to a lower efficiency. This explains the different slopes seen in Fig. 6 [panel (a)], where the CNT sheet response has a slope proportional to f^1 (20 dB/dec), whereas the ITO PAN sheet has a slope closer to $f^{0.5}$ (10 dB/dec) due to its higher HCPUA.^{20,31} This poorer efficiency is also seen in Fig. 6 [panel (b)], where for a similar input power the output SPL is about 20 dB higher for the CNT sheet. It is also seen that the power response slope is in both cases 20 dB/dec, meaning that the SPL output is directly proportional to the input P_{in} as previously recorded in theoretical and experimental literature.³⁵ In spite of the lower thermoacoustic performances, ITO

PAN sheets are interesting materials for technological reasons. In fact, PAN polymers can be easily electrospun and coated with metals.³¹ The ITO coating, in particular, is deposited by radio frequency sputtering and the final film is resistant to relatively high temperatures and quite transparent.³¹

A good agreement of both 1T and 2T models is observed with the experimental data, for frequency and power spectra. This is attributed to the fact that the thickness of the thermophone is small enough so that the 2T approach does not add any significant value to the model. The thickness of the sample is still sufficiently small for the HCPUA to be accurately evaluated by a continuous sheet through a 1T model. This, however, would stop to be true for thicker thermophones.

Finally, it can be noted that the output acoustic power for a spherical radiation on the CNT sheet can be estimated as $4\pi r^2 p_{rms}^2 / \rho C_0 = 42 \times 10^{-9}$ W. Here, the pressure at 1 kHz is $p_{rms} = 10^{65/20} \times 20 \times 10^{-6}$ Pa and $r = 0.03$ m as the measurement was done at 3 cm and not at the standard 1 m distance. The pressure being normalized at 1 W input power, this leads to an efficiency of about $4.2 \times 10^{-6}\%$, which is in the same range as reported in the literature.³¹

C. Thick foam thermophones

Figure 7 shows the measured responses of a MWNT sponge (0.1 mm thick) and of a graphene sponge (0.8 mm thick), together with the corresponding theoretical results. In both cases, the diffraction procedure of Sec. III has been applied. These samples have a thickness one/two orders of magnitude larger

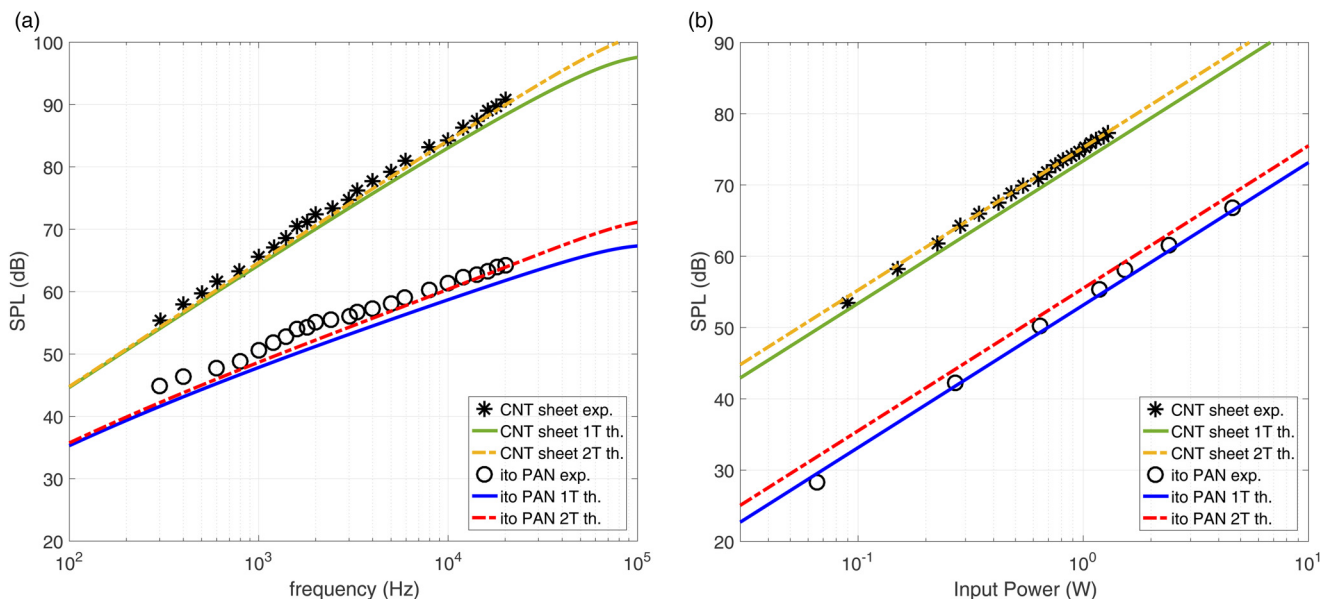


FIG. 6. Comparison of experimental³¹ and theoretical responses of a CNT sheet and an ITO PAN thermophone working in free field at 3 cm distance emission/reception. (a) Power normalized frequency response of the thin film thermophones. (b) SPL response of the thin film thermophones at 3 kHz as a function of the input power. For the 2T model, $N = 10$ has been adopted.

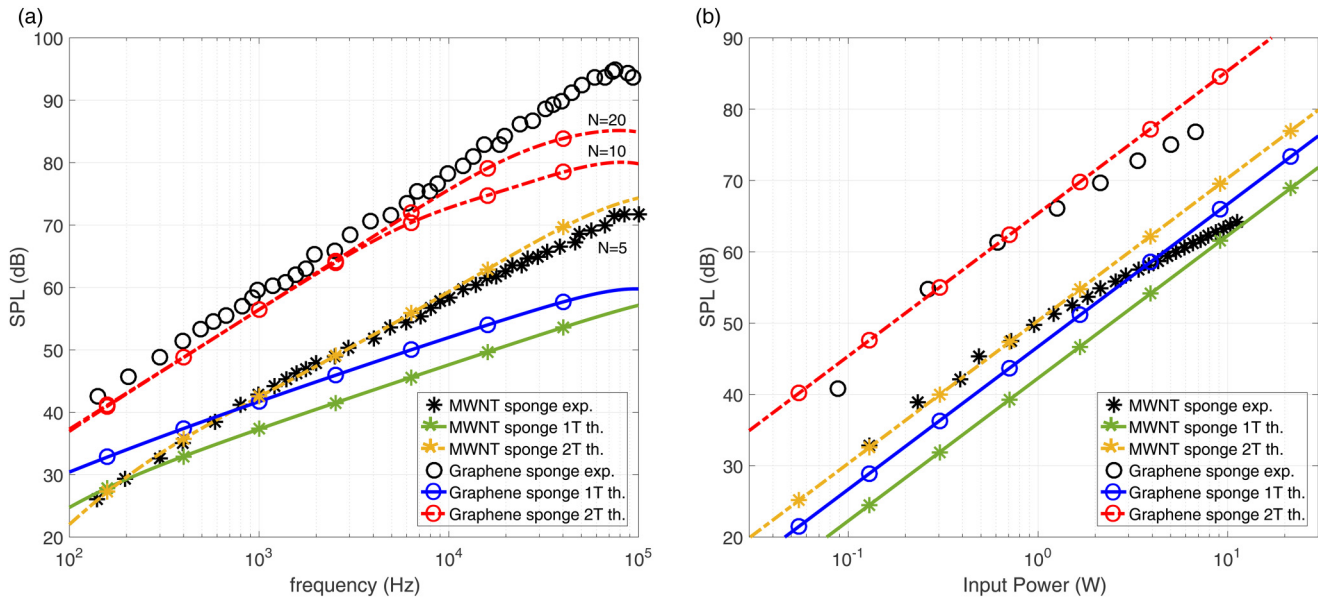


FIG. 7. Comparison of experimental³¹ and theoretical responses of a MWNT sponge and a graphene sponge thermophone working in free field at 3 cm distance emission/reception. (a) Power normalized frequency response of the foam thermophones. (b) SPL response of the foam thermophones at 3 kHz as a function of the input power. For the graphene sponge, the theoretical curve is the same for $N = 10$ and $N = 20$. For the MWNT sponge, $N = 5$ is adopted.

than the previous ones and have a porosity within the range 95%–99%. The experimental frequency spectrum of the graphene sponge displays a slope proportional to f^1 (20 dB/dec), meaning that the efficiency is preserved with respect to the thin film case. Indeed, even if the sample is rather thick, the HCPUA did not increase significantly to reduce the thermophone performances. The high frequency decrease observed is simply due to the diffraction caused by the geometry of the sample. Now, concerning the MWNT sponge experimental frequency response, one observes that for low frequencies (below 1 kHz) the slope is proportional to f^1 (20 dB/dec), and for higher frequencies (between 1 kHz and 100 kHz) the slope becomes proportional to about $f^{0.75}$ (15 dB/dec). Indeed, at high frequencies, the effect of the HCPUA increases and, therefore, the thermoacoustic generation is coherently reduced.²⁰ Interestingly, the same effect exists also in the graphene sponge, but it is not observed here since it appears at higher frequencies because of the different physical parameters.

The important reason for introducing MWNT sponges is that MNWT networks generate an elastically compressible and flexible device.³¹ Moreover, the MWNT sponge fabrication is simple and of low-cost. On the other hand, the use of graphene sponges allows exploiting the exceptional properties of graphene, with a very large exchange surface due to the peculiar sponge geometry. The result is a three-dimensional cross-linked sponge with isotropic physical properties.³¹

In Fig. 7 [panel (a)], using the homogenized parameters of the thermophone shown in Table II,³¹ good agreement is found between the experiments and the 2T theoretical model for the MWNT sponge. A good agreement is also found for low frequencies

between the graphene sponge and the 2T model. However, it is seen that, for higher frequencies, a larger number of interfaces has to be used to reproduce more accurately the experimental behavior. This is explained by the high surface density of the foam within the thermophone layer. Many interfaces need to be used to better represent the large amount of energy provided to the air for high frequencies. On the other hand, the 1T model displays a strongly different spectrum slope with respect to the experiments. This is due to the thickness of the sample. Indeed, the thermal interactions between the air and the thermophone microstructure are not integrated in the 1T model, since it assumes a thick continuous medium, thus artificially increasing the HCPUA. The sound generation inside the pores of the foam is not taken into account since the model is continuous and, therefore, more heat is assumed to be stored while it is actually dissipated in the pores air.

The power spectra of the thick samples are shown in Fig. 7 [panel (b)] and display a different behavior with respect to the thin samples. At low input powers, the SPL of the samples is proportional to P_{in} (20 dB/dec), but for higher input powers, the spectrum is approximately proportional to $P_{in}^{0.75}$ (15 dB/dec). This nonlinear behavior can be interpreted with an increase of the average static temperature inside the pores of the foam and with a consequent efficiency reduction.³¹ It is seen that our model is not able to reproduce this behavior since the average temperature within the pores is fixed *a priori*.

V. CONCLUSIONS

A two-temperature model for describing the thermoacoustic generation of sound by thick foam thermophones has been

elaborated. To do this, the balance equations for a fluid embedded in the foam microstructure of the thermophone were used and combined with the energy balance within the solid foam material. The energetic coupling between solid foam and fluid (typically air) is controlled by a new coefficient, which describes the heat transfer between foam and air in the porous structure. For the sake of simplicity, this model is developed under the hypotheses of one-dimensional geometry and time-harmonic regime. It means that the propagation of fully coupled thermoacoustic plane waves is investigated in the thermophone system. To model the complex microstructure, a series of interfaces are used to represent the contact zone between air and foam, where the energy transfer between the phases occurs. The resulting equations were solved by imposing the continuity of normal stress, particle velocity, temperatures, and the balance of the heat flux at each interface. The calculated velocity was then used to simulate acoustic diffraction from a finite size thermophone using the classical Rayleigh's integral.

Then, the spatial distribution of the main physical variables was studied for both thick and thin thermophones. The results obtained through our two temperature model were compared with the classical model composed of a solid bulk generating layer. It was proven that the output SPL may be different between these models, depending on the thickness of the thermophone. For thin thermophones, 1T and 2T models give similar results but thicker thermophones lead to significant differences in the output SPL. These differences have been explained in terms of the specific features implemented in the two models. Afterward, the frequency and power spectra were compared with experimental results published in the recent literature.³¹ The similar behaviors of the 1T and 2T models for thin thermophones were confirmed and both models were in quite good agreement with the experimental results. Thick thermophones were then investigated. While the 1T model was unable to accurately reproduce the experimental results, the 2T model displayed good agreement from the point of view of both frequency and power spectra. However, it could be further improved since it is unable to represent the losses due to the static temperature rise within the porous structure. It was pointed out that, for complex foamlike structures, it is important to consider the so-called homogenized parameters of the whole sample (solid plus air), which are different from the local parameters of a single foam branch.

In conclusion, the two-temperature model presented in this paper appears to be a first step in modeling thick and nano- or microstructured thermophone systems. The most important point introduced concerns the exchange of energy at any contact surface between air and solid foam. This feature better represents the reality of such systems and is able to reproduce experimental results, which were not understood on the basis of previous models.

ACKNOWLEDGMENTS

This work was funded by the Thales Underwater System and the French DGA (Direction Générale de l'Armement) and is part

of a project developed in collaboration with CINTRA, UMI 3288 CNRS/NTU/THALES (Singapore).

REFERENCES

- ¹P. Lange, *Proc. R. Soc. Lond.* **91**, 239 (1915).
- ²H. Arnold and I. Crandall, *Phys. Rev.* **10**, 22 (1917).
- ³E. Wente, *Phys. Rev.* **19**, 333 (1922).
- ⁴H. Shinoda, T. Nakajima, K. Ueno, and N. Koshida, *Lett. Nat.* **400**, 853 (1999).
- ⁵A. Niskanen, J. Hassel, M. Tikander, P. Maijala, L. Gronberg, and P. Helisto, *Appl. Phys. Lett.* **95**, 163102 (2009).
- ⁶R. Dutta, B. Albee, W. V. D. Veer, T. Harville, K. Donovan, D. Pamoschou, and R. Penner, *J. Phys. Chem. C* **118**, 29101 (2014).
- ⁷H. Tian, D. Xie, Y. Yang, T. Ren, Y. Lin, Y. Chen, Y. Wang, C. Zhou, P. Peng, L. Wang, and L. Liu, *Appl. Phys. Lett.* **99**, 253507 (2011).
- ⁸H. Tian, T. Ren, D. Xie, Y. Wang, C. Zhou, T. Feng, D. Fu, Y. Yang, P. Peng, L. Wang, and L. Liu, *ACS Nano* **5**, 4878 (2011).
- ⁹W. Fei, J. Zhou, and W. Guo, *Small* **11**, 2252 (2015).
- ¹⁰L. Tao, H. Sun, Y. Liu, Z. Ju, Y. Yang, and T. L. Ren, *Appl. Phys. Lett.* **111**, 103104 (2017).
- ¹¹A. Aliev, M. Lima, S. Fang, and R. Baughman, *Nano Lett.* **10**, 2374 (2010).
- ¹²L. Xiao, Z. Chen, C. Feng, L. Liu, Z. Bai, Y. Wang, L. Qian, Y. Zhang, Q. Li, K. Jiang, and S. Fan, *Nano Lett.* **8**, 4539 (2008).
- ¹³M. Daschewski, R. Boehm, J. Prager, M. Kreutzbruck, and A. Harrer, *J. Appl. Phys.* **114**, 114903 (2013).
- ¹⁴P. Torraca, L. Larcher, M. Bobinger, P. Pavan, B. Seeber, and P. Lugli, *J. Appl. Phys.* **121**, 214502 (2017).
- ¹⁵H. Hu, T. Zhu, and J. Xu, *Appl. Phys. Lett.* **96**, 214101 (2010).
- ¹⁶Y. Yin and H. Hu, *AIP Conf. Proc.* **1829**, 020033 (2017).
- ¹⁷H. Hu, D. Wang, and Z. Wang, *AIP Adv.* **4**, 107114 (2014).
- ¹⁸C. Lim, L. Tong, and Y. Li, *J. Sound Vib.* **332**, 5451 (2013).
- ¹⁹L. Tong, C. Lim, S. Lai, and Y. Li, *Appl. Therm. Eng.* **86**, 135 (2015).
- ²⁰P. Guiraud, S. Giordano, O. Bou-Matar, P. Pernod, and R. Lardat, *J. Sound Vib.* **455**, 275 (2019).
- ²¹M. Loeblein, R. Tay, S. Tsang, W. Ng, and E. Teo, *Small* **10**, 2992 (2014).
- ²²J. Auriault and P. Royer, *Int. J. Heat Mass Transfer* **36**, 2613 (1993).
- ²³M. Quintard, M. Kaviany, and S. Whitaker, *Adv. Water Resour.* **20**, 77 (1997).
- ²⁴A. Nouri-Borujerdi, A. Noghrehabadi, and D. Rees, *Int. J. Heat Mass Transfer* **50**, 3244 (2007).
- ²⁵A. d'Hueppe, M. Chandesris, D. Jamet, and B. Goyeau, *Int. J. Heat Mass Transfer* **55**, 2510 (2012).
- ²⁶S. Giordano and F. Manca, *Int. J. Heat Mass Transfer* **78**, 189 (2014).
- ²⁷L. Landau and E. Lifschitz, *Fluid Mechanics*, 3rd ed., Course of Theoretical Physics Vol. 6 (Butterworth Heinemann, Oxford, 1986).
- ²⁸B. Mason, S. Chang, J. Chen, S. Cronin, and A. Bushmaker, *ACS Nano* **9**, 5372 (2015).
- ²⁹F. Pavanello, F. Manca, P. Palla, and S. Giordano, *J. Appl. Phys.* **112**, 084306 (2012).
- ³⁰F. Pavanello and S. Giordano, *J. Appl. Phys.* **113**, 154310 (2013).
- ³¹A. Aliev, N. Mayo, M. Andrade, R. Robles, S. Fang, R. Baughman, M. Zhang, Y. Chen, J. Lee, and S. Kim, *ACS Nano* **9**, 4743 (2015).
- ³²A. Peigney, C. Laurent, E. Flahaut, R. Bacsca, and A. Rousset, *Carbon* **39**, 507 (2001).
- ³³S. Drieschner, M. Weber, J. Wohlketter, J. Vieten, E. Makrygiannis, B. M. Blaschke, V. Morandi, L. Colombo, F. Bonaccorso, and J. A. Garrido, *2D Mater.* **3**, 045013 (2016).
- ³⁴C. Silvestri, M. Riccio, R. H. Poelma, B. Morana, S. Vollebregt, F. Santagata, A. Irace, G. Q. Zhang, and P. M. Sarro, *Nanoscale* **8**, 8266 (2016).
- ³⁵V. Vesterinen, A. Niskanen, J. Hassel, and P. Helisto, *Nano Lett.* **10**, 5020 (2010).